Numerical simulations of magnetohydrodynamic flows driven by a moving permanent magnet

S. Prinz, V. Bandaru, Y. Kolesnikov, D. Krasnov, and T. Boeck

Institut für Thermo- und Fluiddynamik, Technische Universität Ilmenau, Germany

(Received 15 January 2016; published 1 August 2016)

We present results from numerical reconstructions of magnetic obstacle experiments performed in liquid metal flows. The experimental setup consists of an open rectangular container filled with a thin layer of liquid metal (GaInSn). A permanent magnet is installed on a rail beneath the container and is moved with a constant velocity U_0, which in turn induces a flow inside the liquid metal due to Lorentz forces. The setup allows experiments in a parameter range that is accessible by direct numerical simulations (DNS). We present results from realizations with four different parameter sets, covering flows with stable stationary vortex structures in the reference system of the moving magnet as well as time-dependent flow regimes. Although the liquid metal layer is very thin, the flow shows a highly three-dimensional character in the near and in the far wake of the magnetic obstacle. We conclude that the streamline visualization in the experiment (using gas bubbles at the surface of the liquid metal layer) is insufficient to picture the flow structure occurring in the liquid metal. To underpin our conclusions, we introduce a modified numerical model which aims to mimic the movement of these gas bubbles. Although this model is a strong simplification of the highly complicated behavior of bubbles at a fluid-fluid interface, it captures the main effects and provides a good reproduction of the experimental results. Furthermore, transient effects are investigated when the flow is initiated, i.e., when the magnet approaches the container and crosses its front wall. We conclude that the process of vortex formation is accompanied by a decrease of the streamwise component of the Lorentz force compared to the time when the fluid is still quiescent. This decrease occurs only for flows with stable vortex structures, which might be of interest for practical applications like Lorentz force velocimetry. The Lorentz forces obtained from our DNS are in good agreement with the values measured in experiment.

I. INTRODUCTION

An electrically conducting fluid moving relative to a magnetic field is influenced by Lorentz forces [1–3]. This phenomenon occurs in a variety of industrial applications, e.g., stirring and casting of liquid metals, suppression and damping of turbulence in crystal growth, or inductive noncontact flow measurement techniques like Lorentz force velocimetry [4,5]. If a conducting fluid, e.g., liquid metal, moves through a localized, spatially inhomogeneous magnetic field, the flow is affected by Lorentz forces, which brake the flow and act as an obstacle to it. Depending on the physical and geometric parameters, the flow shows some similarities to the purely hydrodynamic flow around a solid obstacle. Therefore, this phenomenon is commonly termed as magnetic obstacle. In the case of a hydrodynamic flow around a solid obstacle, the flow characteristics are completely described by the Reynolds number Re, which is defined as the ratio of inertial to viscous forces. The Reynolds number is given by

$$\mathrm{Re} = \frac{UL}{\nu}, \tag{1}$$

where U and L are the scales for velocity and length, respectively, and ν is the kinematic viscosity of the fluid. Unlike its hydrodynamic counterpart, the flow structure of the magnetic obstacle shows an increased complexity since an additional parameter controls the flow, namely, the Stuart number

N, which describes the ratio of Lorentz forces to inertial forces and is given by

$$N = \frac{\sigma L B^2}{\rho U},$$ (2)

where B is the scale for the magnetic induction and σ and ρ are the electrical conductivity and density of the fluid, respectively.

Due to its broad range of practical applications (e.g., in metallurgical processing), the magnetic obstacle phenomenon has been addressed by a number of recent research works in both numerical (e.g., Refs. [6–12]) and experimental (e.g., Refs. [13,14]) studies. In general, the magnetohydrodynamic flow past a magnetic obstacle can be divided into a variety of different flow regimes.

For example, at relatively high Reynolds numbers, the magnetic obstacle brakes a laminar flow and produces turbulence in the near and far wake. This has a direct application, e.g., in metallurgy to trigger turbulence and therefore to enhance as well as to control mixing processes. For example, Tympel *et al.* [10] presented a comprehensive numerical study where they used a magnetic point dipole as a simplified magnetic obstacle and systematically studied its influence on pressure-driven magnetohydrodynamic flow in a square duct. They presented realizations that span over a broad parameter space from stationary flow at low Reynolds numbers to transitional and turbulent flows at moderate Reynolds numbers. Among other things, they found that a spanwise orientation of the dipole is the configuration with the most effective production of turbulence. Closer to practical applications are studies where the magnetic obstacle is modeled by the field of permanent magnets with a finite spatial extension, as done in Kenjereš [9]. The author used single and multiple pairs of permanent magnets above and beneath conducting flows inside closed ducts. In this work, the Stuart number is varied between $N = 0$ and 50 at a fixed Reynolds number (Re = 1000), and it is concluded that a configuration of multiple magnets may be used in practical applications to enhance mixing of passively transported scalars due to the generation of turbulence.

A qualitatively different flow regime occurs for smaller Reynolds numbers and sufficiently strong magnetic fields. In this regime, different stable vortex structures may occur, which seem to be a unique feature of the magnetic obstacle phenomenon. One of them is the so-called six-vortex structure, which is described in various research works [6–8,11]. The six-vortex structure consists of three symmetric pairs of vortices: in the inner region of the magnetic obstacle (i.e., where the highest values of the magnetic field are present inside the flow domain) two so-called magnetic vortices form. Analogous to the flow around a solid obstacle, a wake may form with an area of recirculation [11]. Because these vortices show the same direction of rotation, two smaller vortices with reversed rotation direction occur between them to provide a continuous flow [7]. These vortices are commonly termed as connecting vortices. For much lower Reynolds numbers, no zone of recirculation exists in the wake, and only two magnetic vortices occur in the inner region of the magnetic obstacle.

In Votyakov *et al.* [7], the different flow regimes were divided into three groups: (1) for small Lorentz forces compared to viscous forces, no stable vortices form in the flow, (2) for high Lorentz forces and small inertia, two magnetic vortices occur, and (3) for high Lorentz and inertial forces, the six-vortex structure forms.

To our knowledge, there exists no study where results from numerical simulations and experimental data are directly compared for the same parameters. This is the primary motivation for the present paper. The experimental results are already published in Kolesnikov and Thess [14] and Samsami *et al.* [13]. In both works, the same experimental setup is used. Unlike the above mentioned configurations of numerical studies, they use an open container filled with GaInSn, an eutectic alloy which is liquid at room temperature, and let a permanent magnet move beneath the container. Since the velocity of the magnet can be arbitrarily small, this setup allows experiments for parameters accessible by means of direct numerical simulations. With this paper, we want to provide a detailed comparison between experimental and numerical results which allows a deeper
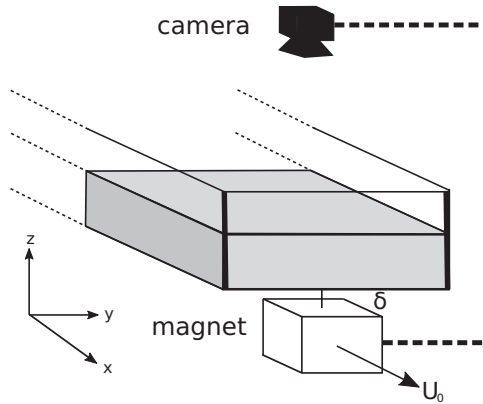
FIG. 1. Schematic of the experimental setup.

insight into the fundamental structure of the flow. Furthermore, we use our numerical method to look beyond the experimental study by analyzing the transient development of the flow.

This paper is structured as follows: in Sec. II the experimental setup, the physical model, the numerical method and setup are explained. In Sec. III we present our results divided into three parts: in Sec. III A, we analyze results from our DNS of the flow structure when the flow is fully evolved, i.e., the main properties of the flow are independent of time. In Sec. III B, we present numerical results of transient effects, i.e., when the flow is initiated. In Sec. III C, we present a detailed comparison between experimental and numerical results. Concluding remarks are given in Sec. IV.

II. PROBLEM DEFINITION

A. Experimental setup

The experimental setup is the same as presented in the work of Samsami *et al.* [13] and Kolesnikov and Thess [14]. Figure 1 shows a sketch of the present problem. The open rectangular container has the dimensions of 1200 mm × 100 mm for length (x) × width (y) and is filled with the eutectic alloy GaInSn to a height of 10 mm (z). The dimensions of the magnet are 30 mm × 40 mm × 20 mm for length (x) × width (y) × height (z). The magnet moves on a rail below the container in the direction of the x coordinate. Therefore, the x direction is called streamwise and the y direction spanwise direction. The distance δ from the surface of the magnet to the bottom of the container is 8 mm. GaInSn has a melting temperature of 10.5 °C, density $\rho = 6363 \, \text{kg} \, \text{m}^{-3}$, electrical conductivity $\sigma = 3.46 \times 10^6 \, \Omega^{-1} \, \text{m}^{-1}$, and a kinematic viscosity $\nu = 4 \times 10^{-7} \, \text{m}^2 \, \text{s}^{-1}$. The length scale L_0 is chosen as the thickness of the liquid metal layer (10 mm), and the velocity scale is the velocity of the magnet U_0. In the experiments, the magnet velocity U_0 is varied from 5 to 44 mm s^{-1}.

Although both works use the same experimental setup, measured values for the magnetic field differ. In Samsami *et al.* [13], the maximal magnitude of the magnetic field at the surface of the liquid metal container is reported as $B = 0.137 \, \text{T}$, whereas this value is stated as $B = 0.125 \, \text{T}$ in the work of Kolesnikov and Thess [14]. Furthermore, the normalization value of the magnetic field B_0 is different. In Samsami *et al.* [13], the magnetic field is normalized by its maximal magnitude at the surface of the liquid metal layer, whereas in Kolesnikov and Thess [14] the maximal magnitude in the middle plane of the liquid metal layer is used. Since we assume that the mismatch of measured values is due to a small deflection of the rail on which the magnet moves, we decided to adapt the setup of Kolesnikov and Thess [14] for the numerical reconstruction (see Sec. II D). Therefore, the normalization value of the magnetic field is $B_0 = 0.1513 \, \text{T}$ in the middle layer of the liquid metal.

Streamlines are visualized by a layer of dilute hydrochloric acid solution of 4% concentration above the liquid metal layer. The acid layer has a thickness of about 4 mm. The density of the

TABLE I. Parameter space of the experimental and numerical realizations. The only varied quantity is the velocity of the magnet U_0.

$\text{Re} = \dfrac{U_0 L_0}{\nu}$	$N = \dfrac{\sigma L_0 B_0^2}{\rho U_0}$	U_0 (mm s^{-1})
125	24.91	5
250	12.45	10
550	5.66	22
1100	2.83	44

hydrochloric acid solution is approximately the same as that of water. Due to a chemical reaction, small gas bubbles form at the interface between the liquid metal and the acid solution. Because of surface tension, these gas bubbles stick at the interface and thus help visualize the flow structure at the surface of the liquid metal. A camera is installed above the container, which moves together with the magnet while recording the streamline pattern.

We present the results of four experiments with parameters as shown in Table I.

B. Governing equations and boundary conditions

In the present case, the magnetic field of the induced currents is small compared to the imposed magnetic field of the magnet, and hence the influence of the flow on the magnetic field can be neglected (quasistatic approximation) [1,2]. Using U_0, L_0, L_0/U_0, ρU_0^2, B_0, and $L_0 U_0 B_0$ as scales for velocity, length, time, pressure, magnetic field, and electrical potential, respectively, the full set of nondimensional magnetohydrodynamic equations for incompressible flow in the quasistatic approximation reads [15]

$$\boldsymbol{\nabla} \cdot \mathbf{u} = 0, \tag{3}$$

$$\frac{\partial \mathbf{u}}{\partial t} + (\mathbf{u} \cdot \boldsymbol{\nabla})\mathbf{u} = -\nabla p + \frac{1}{\text{Re}}\nabla^2 \mathbf{u} + N(\mathbf{j} \times \mathbf{B}), \tag{4}$$

$$\mathbf{j} = -\boldsymbol{\nabla}\phi + (\mathbf{u} \times \mathbf{B}), \tag{5}$$

$$\nabla^2 \phi = \boldsymbol{\nabla} \cdot (\mathbf{u} \times \mathbf{B}). \tag{6}$$

Here $\mathbf{u}$ is the velocity field $[\mathbf{u} = (u,v,w)]$ in the reference system of the laboratory, p the pressure, $\mathbf{j}$ the electrical current density, $\mathbf{B}$ the imposed magnetic field of the magnet, and ϕ the electrical potential.

For the present work, Ohm's law (5) and the Poisson equation for the electrical potential (6) have to be modified, because only the motion of the fluid relatively to the magnetic field is considered (see Appendix A for a detailed derivation):

$$\mathbf{j} = -\boldsymbol{\nabla}\phi + (\mathbf{u} - \mathbf{u}_0) \times \mathbf{B}, \tag{7}$$

$$\nabla^2 \phi = \boldsymbol{\nabla} \cdot [(\mathbf{u} - \mathbf{u}_0) \times \mathbf{B}]. \tag{8}$$

Here $\mathbf{u}_0 = u_0 \mathbf{e}_x$ ($u_0 = 1$) is the velocity of the magnet. The imposed magnetic field of the permanent magnet is computed by an analytical solution presented in Furlani [16] and reads in dimensional form

$$\mathbf{B}^{\text{dim}}(x,y,z) = \frac{\mu_0 M_s}{4\pi} \sum_{k=1}^{2} (-1)^k \int_{y_1}^{y_2} \int_{x_1}^{x_2} \frac{[(x-x')\mathbf{x} + (y-y')\mathbf{y} + (z-z_k)\mathbf{z}]}{[(x-x')^2 + (y-y')^2 + (z-z_k)^2]^{-3/2}} \, dx' \, dy', \tag{9}$$

where μ_0 is the magnetic permeability of vacuum, M_s the surface magnetization of the magnet; (x_1,x_2), (y_1,y_2), and (z_1,z_2) are the coordinates of the magnet's corners; $\mathbf{x}$, $\mathbf{y}$, and $\mathbf{z}$ represent the surface normals in the x, y, and z direction, respectively.

The boundary conditions for the velocity are of no-slip type for the solid bottom $\Gamma_{z,b}$ and the solid side walls Γ_x and Γ_y:

$$\mathbf{u}|_{\Gamma_{z,b}} = \mathbf{u}|_{\Gamma_x} = \mathbf{u}|_{\Gamma_y} = 0. \tag{10}$$

Since our numerical method is not able to consider free surfaces, we have to approximate the surface of the liquid metal as a planar free-slip boundary condition for the velocity at the surface $\Gamma_{z,s}$, where

$$w|_{\Gamma_{z,s}} = 0\,, \quad \left.\frac{\partial u}{\partial z}\right|_{\Gamma_{z,s}} = 0, \quad \text{and} \quad \left.\frac{\partial v}{\partial z}\right|_{\Gamma_{z,s}} = 0. \tag{11}$$

All boundaries are set to be electrically insulating:

$$\mathbf{j} \cdot \mathbf{n}|_\Gamma = 0, \tag{12}$$

where $\mathbf{n}$ is the surface normal unit vector. Therefore, the boundary conditions for the electric potential ϕ have to be defined according to Eqs. (7) and (12). For the streamwise boundaries Γ_x, we have

$$\left.\frac{\partial \phi}{\partial x}\right|_{\Gamma_x} = 0. \tag{13}$$

For the side walls Γ_y in a spanwise direction, we have

$$\left.\frac{\partial \phi}{\partial y}\right|_{\Gamma_y} = u_0 B_z, \tag{14}$$

and for the bottom wall $\Gamma_{z,b}$

$$\left.\frac{\partial \phi}{\partial z}\right|_{\Gamma_{z,b}} = -u_0 B_y. \tag{15}$$

The boundary condition for the electrical potential at the surface $\Gamma_{z,s}$ reads

$$\left.\frac{\partial \phi}{\partial z}\right|_{\Gamma_{z,s}} = -(u_0 - u)B_y - v B_x. \tag{16}$$

C. Numerical method

For the numerical solution of the governing equations, we use two different versions of a DNS code presented in Krasnov *et al.* [15]. Both versions of the code discretize the governing equations on a regular grid by an explicit finite-difference scheme of second order. To make the numerical method conservative for mass, momentum, and electrical current, a scheme proposed in Morinishi *et al.* [17] is adopted in which the velocity and current fluxes are computed and stored midway between the collocated points of the solution variables $\mathbf{j}$, p, and $\mathbf{u}$. For time discretization, a fully explicit Adams-Bashforth (backward) differentiation method is adopted. The incompressibility condition is incorporated by a standard Chorin-type projection method by solving the Poisson problem for the pressure p. To resolve the thin magnetohydrodynamic boundary layers, the computational grid can be strongly clustered along the wall-normal direction by a coordinate transformation according to

$$y = \frac{\tanh(\alpha_y \eta)}{\tanh(\alpha_y)} \quad \text{and} \quad z = \frac{\tanh(\alpha_z \xi)}{\tanh(\alpha_z)}\,, \tag{17}$$

where y and z are the transformed nonuniform coordinates of the uniform grid coordinates η and ξ. The coefficients α_y and α_z determine the degree of clustering in the y and z directions, respectively. Since the standard version of the code applies the cosine transformation in the x direction to solve
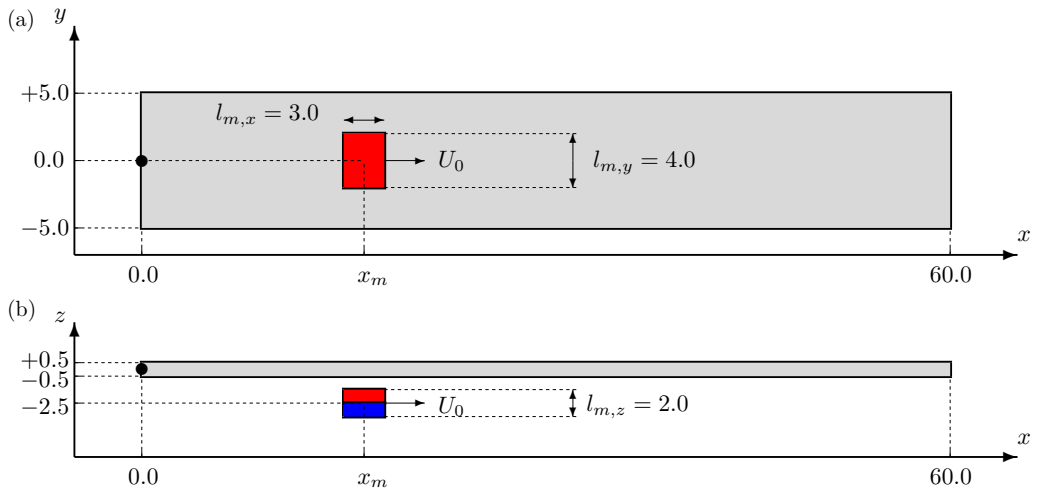
FIG. 2. Computational domain of solver A; all values are in nondimensional units. The dot refers to the origin of the coordinate system; $l_{m,x}$, $l_{m,y}$, and $l_{m,z}$ are the dimensions of the magnet in the x, y, and z direction, respectively; x_m is the variable position of the magnet.

the Poisson equations for pressure p and electrical potential ϕ, the grid is uniformly spaced in this direction (see Zikanov *et al.* [18] for more details).

The aforementioned codes differ in terms of the solution of the Poisson equations. The first code (solver A) solves the Poisson equations in Fourier space by applying the cosine transform in the streamwise direction while utilizing the Fishpack library [19]. Fishpack is a direct solver based on the cyclic reduction method and can favorably be parallelized by domain decomposition. However, the considered functions should be smooth in the direction of transformation to avoid oscillations that contaminate the numerical solution. This so-called Gibbs phenomena may occur when the magnet is close to the streamwise (x) walls Γ_x, since its magnetic field and the boundary conditions for the electrical potential (13) produce sharp gradients in the right hand side of Eq. (8). To avoid the Gibbs phenomena, solver A is used only when the magnet is at a sufficient distance from the streamwise walls. Therefore, solver A is used to study effects when the flow is fully evolved.

The second code (solver B) solves both Poisson equations for p and ϕ by applying the Mudpack library [20]. Mudpack is based on the multigrid technique. Since Mudpack does not have the constraints of the Fourier space, it can be used to study effects when the magnet is close to the streamwise walls or even passes them. However, the multigrid technique is inconvenient for parallelization via domain decomposition. Therefore, our implementation of solver B is restricted to shared-memory parallelization. To save computational resources, the computational domain is shortened in the streamwise direction and the grid is coarser than that for computations with solver A (see next section). We use solver B to study transient effects when the magnet approaches the container and crosses the streamwise front wall.

D. Numerical setup

For the setup of solver A, our preliminary results showed that the flow has sufficient time to evolve in the first half of the computational domain (i.e., between $x = 0$ and $600\,\text{mm}$; see Sec. III A). Therefore, we reduce the computational domain to half the length of the experimental domain to save computational resources. Figure 2 shows a schematic view of the computational domain in nondimensional units. The starting position of the magnet's center is $x_m = 5.0$, $y_m = 0.0$, and $z_m = -2.5$.
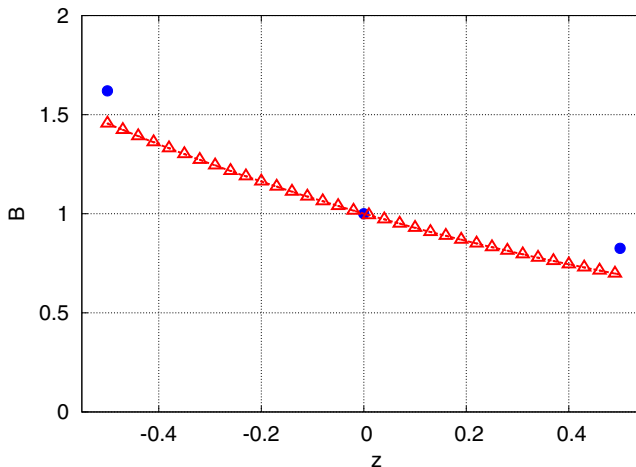
FIG. 3. Nondimensional vertical profile of the magnetic field magnitude above the center of the magnet obtained from Eq. (9), ranging from the bottom of the computational domain at $z = -0.5$ to its surface at $z = 0.5$. The blue dots correspond to the nondimensional measured values reported in Kolesnikov and Thess [14].

Since we assume a small deflection of the rail on which the magnet moves, we decided to add 2 mm to the gap between magnet and liquid metal container. Figure 3 shows the vertical profile of the nondimensional magnetic field magnitude obtained from Eq. (9) above the center of the magnet. The blue dots refer to the nondimensional measured values reported in Kolesnikov and Thess [14]. Unfortunately, there is no systematic measurement of the spatial distribution of the magnetic field reported. We stress that regarding the comparison of the experimental and numerical results, a possible discrepancy between the measured and the calculated magnetic field remains a source of uncertainty.

The computational domain is discretized by a regular grid with $1024 \times 256 \times 32$ points for $N_x \times N_y \times N_z$. The parameters for grid clustering [Eq. (17)] are set to $\alpha_y = \alpha_z = 2.0$ in the y and z directions. A detailed grid independence study is presented in Appendix B.

A schematic view of the computational domain for simulations with solver B is given in Fig. 4. Since we are interested only in the effects at the onset of the flow, we further shorten the computational domain in the x direction to 40.0 (i.e., 400 mm in dimensional units). The starting position of the magnet's center on the x coordinate is changed to $x_m = -3.0$. With this setup we want to study the effects when the magnet approaches the container, and the flow starts to evolve. Due to the extra computational time of solver B and the shortened model size, we restrict ourselves to a coarser computational grid as compared to that of solver A. The grid has $512 \times 128 \times 32$ points for $N_x \times N_y \times N_z$, with a degree of clustering set to $\alpha_y = \alpha_z = 1.0$. Details on grid sensitivity with this solver are given in Appendix B. Profiles of the normalized magnetic field obtained from the analytical solution [Eq. (9)] are shown in Fig. 5.

III. RESULTS AND DISCUSSION

In this section, numerical results are presented and compared with those from the experiments. The section is structured into three parts. At first, results from the numerical simulations are presented when the flow is fully evolved (solver A). After this, results from numerical simulations of the transient case are presented (solver B). Finally, the numerical results are compared to the experiments published in Kolesnikov and Thess [14]. All results presented in this section refer to the reference system of the moving magnet, i.e., they correspond to the velocity field $\mathbf{u} - \mathbf{u}_0$.
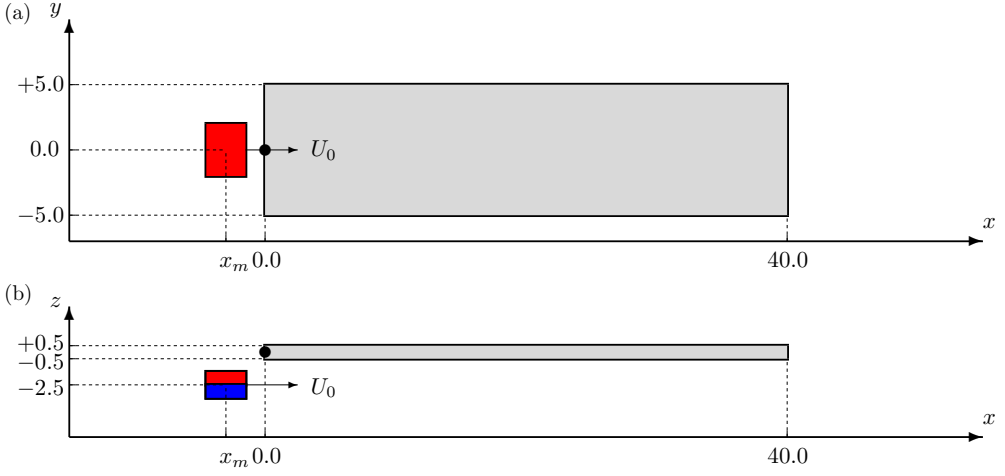
FIG. 4. Computational domain of solver B; all values are in nondimensional units. The dot refers to the origin of the coordinate system. The domain is shortened to a length of 40 (400 mm in dimensional units); x_m is the variable position of the magnet.

A. Fully evolved flow (solver A)

To illustrate the flow structure, three-dimensional instantaneous streamlines together with the vortex structure obtained by the so-called λ_2 criterion [21] are presented for each case.

The λ_2 criterion visualizes the vortex structure by plotting isosurfaces of the second largest eigenvalue of the matrix

$$\Lambda_{ij} = S_{ik}S_{kj} + \Omega_{ik}\Omega_{kj}, \tag{18}$$

where S and Ω are the symmetric and the antisymmetric part of the velocity gradient tensor $\nabla\mathbf{u}$, i.e.,

$$S_{ij} = \frac{1}{2}\left(\frac{\partial u_i}{\partial x_j} + \frac{\partial u_j}{\partial x_i}\right) \quad \text{and} \quad \Omega_{ij} = \frac{1}{2}\left(\frac{\partial u_i}{\partial x_j} - \frac{\partial u_j}{\partial x_i}\right). \tag{19}$$

For the ease of visualization, only selected streamlines are presented to show the main flow structure inside and in the wake of the magnetic obstacle. All results in this section are shown when
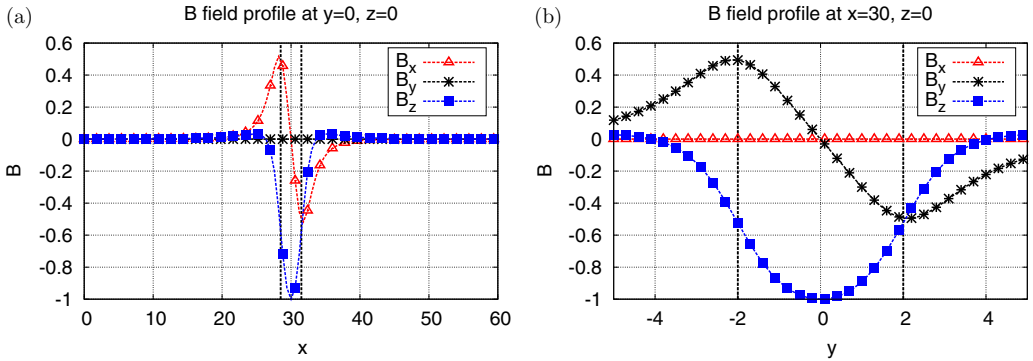
FIG. 5. Profiles of the magnetic field obtained from Eq. (9) (a) along the x direction and (b) along the y direction. Dashed lines mark the start and end points of the magnet with respect to the presented coordinates. Values are given in nondimensional units.
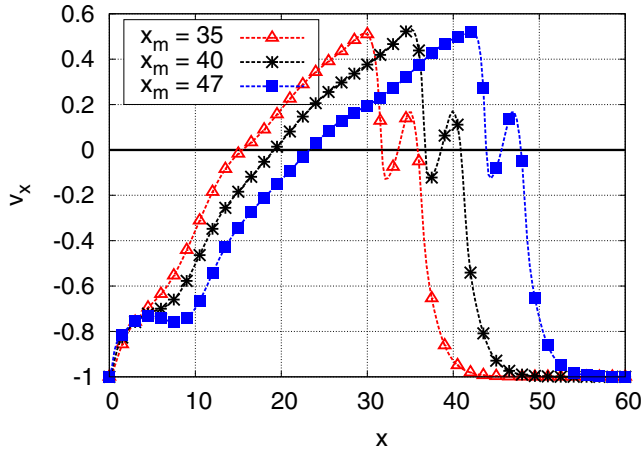
FIG. 6. Streamwise velocity profiles for Re = 250 and $N = 12.45$ at different magnet positions; x_m is the position of the magnet's center in the x direction. The profiles are extracted along the centerline at the surface, at $y = 0$ and $z = 0.5$.

the magnet reaches $x_m = 47.0$. By the time the magnet reaches this position, the flow has sufficient time to develop, which also justifies the bisection of the computational domain length compared to the experimental model size (see Fig. 6). A detailed physical discussion of the streamwise velocity profiles like shown in Fig. 6 is provided in Sec. III A.

In the following, we analyze the results, starting from the lowest Reynolds number and therefore, the highest Stuart number (i.e., Re = 125 and $N = 24.91$). Figure 7(a) shows that the flow forms a six-vortex structure. Two pronounced magnetic vortices are present directly above the permanent magnet (i.e., the inner region of the magnetic obstacle).

In this region, the Lorentz force, which acts contrary to the flow, is maximal and produces a pressure difference between the front and the back of the magnetic obstacle. This provides a symmetrical flow around the obstacle and the formation of two vortices inside the magnetic obstacle.

Further downstream the magnetic obstacle, two small connecting vortices follow, which are almost enclosed by the magnetic vortices. In the wake, two stable attached vortices appear. Although this result is in good agreement with previous studies, some properties should be examined in more detail. Figures 8(a) and 8(b) show a close-up of the same vortex structure. This illustration clearly shows that the magnetic vortices appear across the complete model space in vertical direction. Unlike the magnetic vortices, the attached vortices in the wake clearly show a different character. The streamlines start in the bulk of the flow. With growing distance from the magnetic obstacle the streamlines slowly ascend to the surface and reconnect to the magnetic obstacle. Unlike the magnetic vortices, the attached vortices show a highly three-dimensional character.

Similar effects appear for the next Reynolds number, i.e., for Re = 250 and $N = 12.45$ [Fig. 7(c)]. Again, the streamline pattern shows a six-vortex structure that differs only slightly from the previous one. Strong similarities between both simulations can also be seen in the vortex structure obtained by the λ_2 criterion in Figs. 7(b) and 7(d). However, for Re = 250 and $N = 12.45$, small-scale vortical structures appear in the region downstream of the magnetic obstacle. Figures 8(c) and 8(d) show the close-up of the flow structure. Again, the magnetic vortices evolve across the entire model space in vertical direction. Additionally, the axis of the magnetic vortices shows a small inclination with respect to the surface, indicating a helical character that is caused by the increased velocity of the magnet. The attached vortices in the wake also rise from the bulk to the surface, but are penetrating deeper into the model space compared to the previous case.

The results described above can be interpreted as follows. A fluid particle located inside the magnetic obstacle will be transported to the bottom by the helical structures. There it will lose its
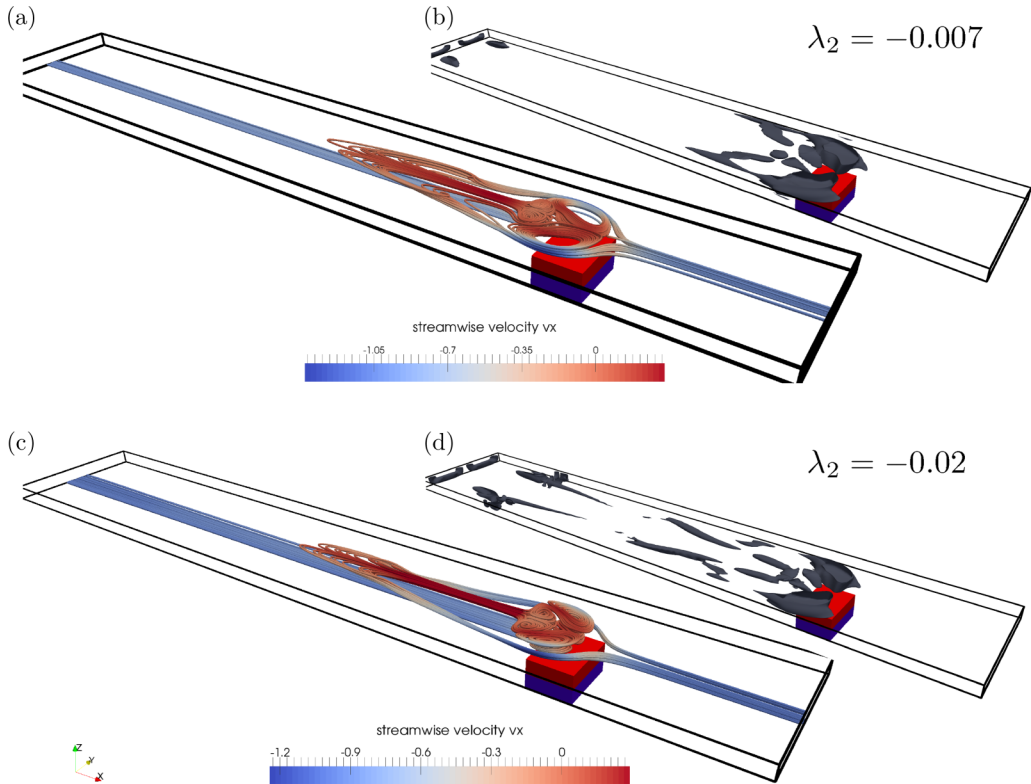
FIG. 7. Fully evolved flow (solver A): instantaneous three-dimensional streamlines (a) and vortex structure (b) obtained by the λ_2 criterion for Re = 125 and N = 24.91 and for Re = 250 and N = 12.45 [(c) and (d), respectively]. Streamlines are seeded in such a way as to demonstrate the main flow structure.

kinetic energy due to dissipation. The attached vortices compensate this effect by transporting fluid from the bulk of the flow to the surface and from there back to the inner region of the magnetic obstacle. Although the three-dimensional character and the helical structure of the magnetic vortices are also reported in Votyakov *et al.* [6], we observe some fundamental differences for our setup. The analogy to the wake that appears in flows around solid obstacles is misleading in this case, because the attached vortices seem to have the additional function of rebalancing the mass deficit occurring due to the helical character of the magnetic vortices. In addition, the free surface influences the flow.
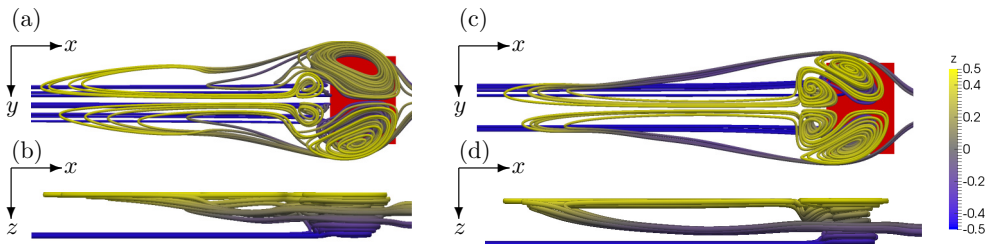
FIG. 8. Fully evolved flow (solver A): instantaneous three-dimensional streamlines viewed from different perspectives, (a) and (b) Re = 125 and N = 24.91 and (c) and (d) for Re = 250 and N = 12.45. For a better visualization, streamlines are colored by their vertical coordinate z, and in the side views (b), (d), the visual aspect ratio x/z is changed by a factor of 1/2.
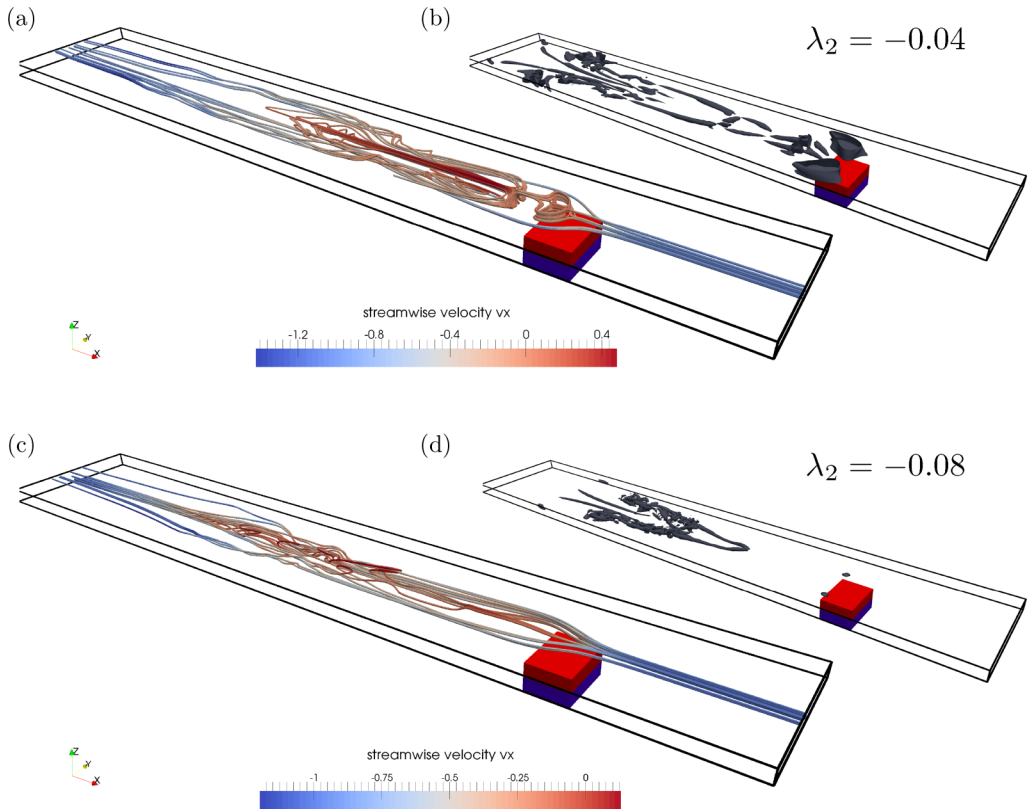
FIG. 9. Fully evolved flow (solver A): instantaneous three-dimensional streamlines (a) and vortex structure (b) obtained by the λ_2 criterion for Re $= 550$ and $N = 5.66$ and for Re $= 1100$ and $N = 2.83$ [(c) and (d), respectively]. Streamlines are properly chosen to demonstrate the main flow structure.

The reduced friction at the free surface gives rise to the attached vortices to ascend to the surface where regions with highly pronounced recirculation appear.

For an increased ratio of inertia to Lorentz forces, i.e., for Re $= 550$ and $N = 5.66$ [Fig. 9(a)], the flow regime is obviously different. Two small vortices appear in the inner region of the magnetic obstacle, but no stable vortices form in its wake. However, recirculation can be seen in the wake, but the flow is characterized by smaller vortical structures in contrast to the case of stable vortices. This can also be seen in the plot for the λ_2 criterion [Fig. 9(b)]. Similar to the previous case, these small vortical structures are distributed across the entire model space downstream from the obstacle. A close-up of the flow structure above the magnet viewed from the top is provided in Fig. 10(a).

For the simulation of the highest Reynolds number, and therefore lowest Stuart number, Re $= 1100$ and $N = 2.83$ [Fig. 9(c)], no stable vortex structure is present in the flow. The vortical structures visualized by the λ_2 criterion [Fig. 9(d)] show a horseshoe-like structure similar to that observed in the work of Tympel *et al.* [10] for turbulent regimes. The areas of small vortical structures are located in the far wake of the magnetic obstacle. For these parameters, the ratio of Lorentz forces to inertial forces is too small to maintain a flow pattern with stable stationary vortices. A close-up of the flow structure above the magnet viewed from the top is provided in Fig. 10(b).

A more detailed insight into the flow is presented in Fig. 11, where profiles of the streamwise relative velocity components are presented for each simulation at different depths, ranging from the surface at $z = 0.5$ to slightly above the bottom at $z = -0.4$. All profiles are extracted at $y = 0$ and correspond to the same position of the magnet as shown in Figs. 7–10. Recirculation occurs if the
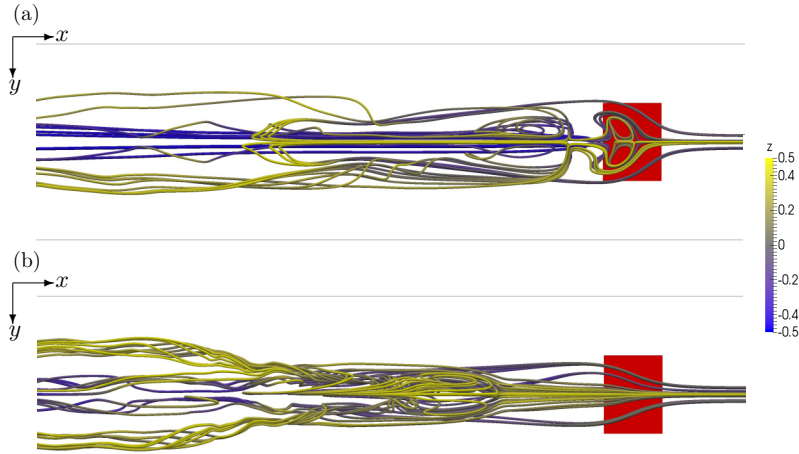
FIG. 10. Fully evolved flow (solver A): instantaneous three-dimensional streamlines viewed from the top, (a) Re = 550 and N = 5.66 and (b) Re = 1100 and N = 2.83. For a better visualization, streamlines are colored by their vertical coordinate z.
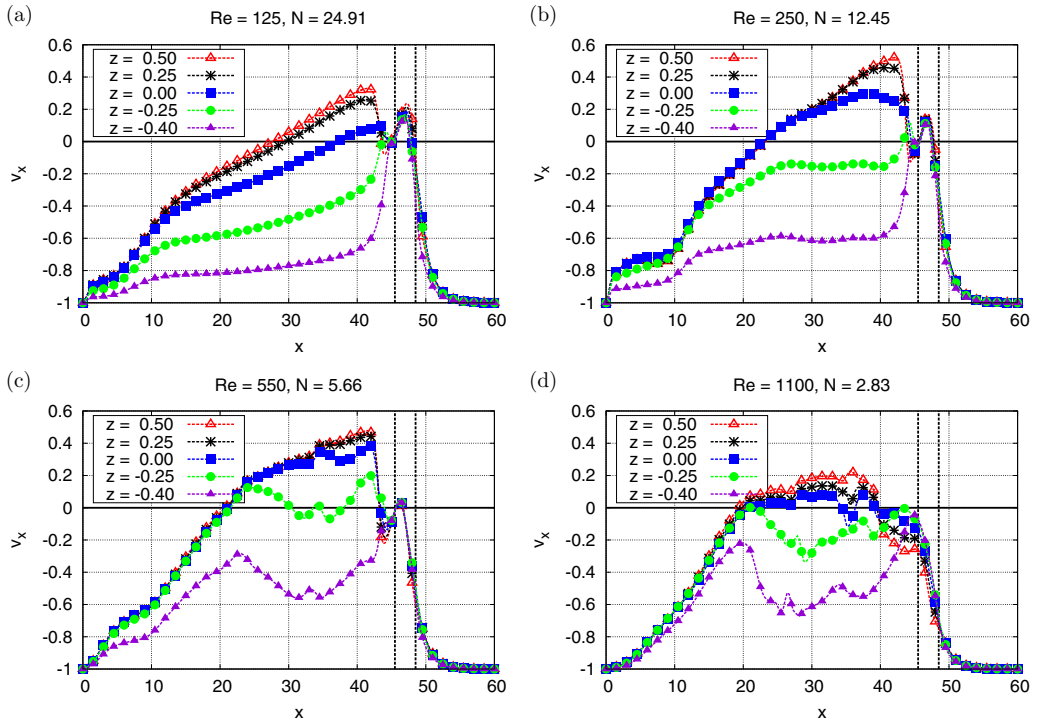
FIG. 11. Fully evolved flow (solver A): profiles of the streamwise velocity component v_x for all four simulations at different depths, ranging from the surface at $z = 0.5$ to slightly above the bottom at $z = -0.4$. Profiles are extracted for $y = 0$ (middle line). The position of the magnet's center is $x_m = 47.0$. The position of the front and back wall of the magnet is marked by the dashed vertical lines.

streamwise velocity exceeds zero. All four simulations have in common that the streamwise velocity component is apparently independent of depth upstream and above the magnetic obstacle. This is consistent with the previously drawn conclusions that the magnetic vortices in the inner region of the obstacle are almost uniformly distributed along the vertical direction. In the wake of the magnetic obstacle, all four simulations show a strong depth-dependent streamwise velocity component, which underpins the three-dimensional character of the wake.

For Re = 125 and $N = 24.91$, the connecting vortices can be seen in the slightly negative values directly behind the magnet at $x = 45.5$. The velocity profile near the solid bottom ($z = -0.4$) decreases rapidly due to dissipation in the boundary layer. The first profile that shows slight recirculation is at $z = 0.0$. Intense recirculation is visible only in the shallow regions beneath the surface at $z = 0.25$ and $z = 0.5$. At the surface, recirculation is present upto $x \approx 30$, which can be used as a measure of the wake's length.

For Re = 250 and $N = 12.45$, the velocity profiles are approximately identical to the previous case upstream and inside the magnetic obstacle, as well as for the connecting vortices. Significant differences appear in the wake. In general, the profiles become less smooth. Further, the values of the relative velocity are higher, and the recirculation is clearly present at the middle of the model space at $z = 0.0$.

For Re = 550 and $N = 5.66$, all velocity profiles become more fluctuating. It is remarkable that regions of recirculation in the wake appear (at least) until a depth of $z = -0.25$. Even close to the solid bottom, the velocity profile shows relatively high values up to $v_x \approx -0.3$ in the far wake of the obstacle. Although there are no stable vortex structures in the wake [see Fig. 9(a)], the constant high values of the streamwise velocity at the surface indicate that a well-ordered structure of recirculation still appears.

For the highest Reynolds number and the lowest Stuart number, i.e., for Re = 1100 and $N = 2.83$, the velocity profiles clearly show that no stable vortex structure occurs, neither inside the magnetic obstacle nor in its wake. The absolute values of the relative velocity drop and less intense parts of recirculation appear until a depth of at least $z = 0.0$. Clearly, the velocity decreases with depth, but the difference between the profiles becomes smaller. In the wake, deeper regions of the model space are more strongly affected by the influence of the magnetic obstacle than compared to the previous cases.

B. Transient development (solver B)

In this section, results from the investigation of the transient flow development (solver B) are presented. For that, we evaluate the Lorentz forces acting when the magnet approaches the container (Fig. 12) and compare them with the instantaneous flow structure illustrated by three-dimensional streamlines (Fig. 13). For the sake of comparison, we also calculate the Lorentz forces **f** acting on the magnet for a stationary solid slab (i.e., the velocity of the fluid is forced to be zero). The starting position of the magnet is changed to $x_m = -3.0$. At $x_m = 0$, the center of the magnet crosses the front wall of the container.

Let us first consider the streamwise Lorentz forces f_x for all fluid simulations [Fig. 12(a)]. In all cases, the Lorentz force increases when the magnet approaches the container. The curves of the nondimensional Lorentz forces are almost identical until shortly before the center of the magnet reaches the front wall at $x_m \approx 0$. This indicates that at this stage the fluid is still mostly quiescent. Shortly after the center of the magnet crossed the wall, the curves diverge and each reaches a (local) maximum at about $x_m \approx 0.6$. The appearance of the maximum in the Lorentz force indicates that at this position of the magnet the magnetic and attached vortices, which improve the flow around a magnetic obstacle, do not exist yet. Indeed, at this stage the flow starts to evolve, which can be seen in the left column of Fig. 13. At this stage, the magnet nearly completely passed the front wall and the magnetic field overlaps the computational domain. Since the fluid begins to move with a slight delay, the relative velocity between the moving magnetic field and the almost quiescent fluid is maximal, which results in a maximal Lorentz force. Following this, the curves decrease for all simulations
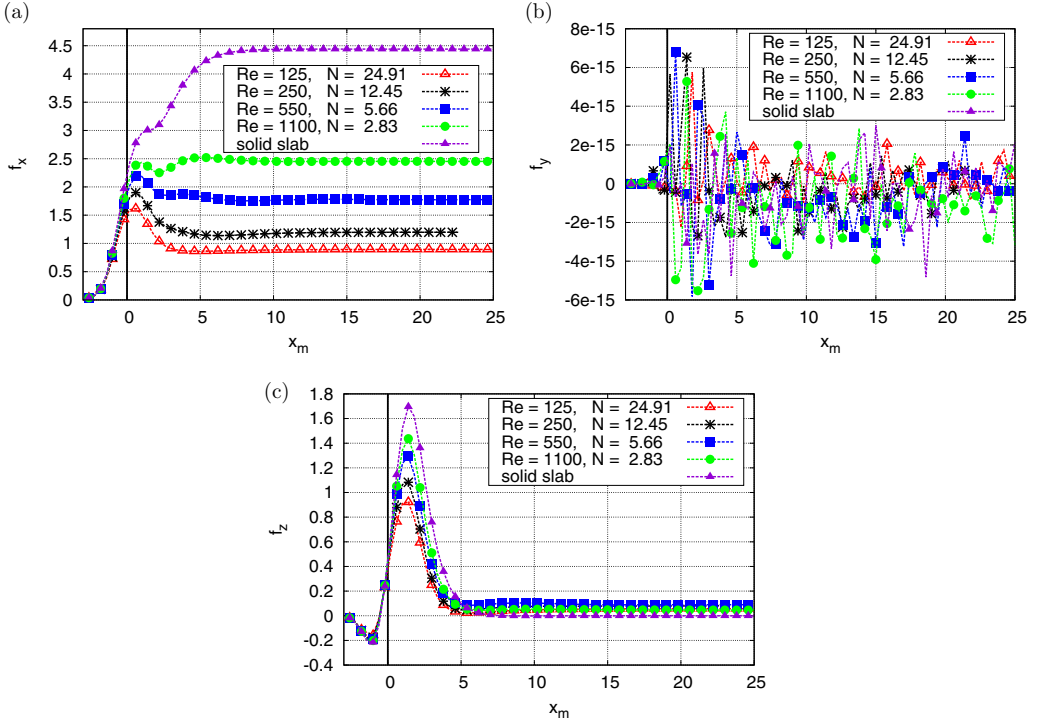
FIG. 12. Transient development (solver B): x, y, and z component of the Lorentz forces depending on the position of the magnet's center x_m. At $x_m = 0$ the magnet's center crosses the streamwise (front) wall of the container.

with stable vortex structures (i.e., for Re = 125 and $N = 24.91$, Re = 250 and $N = 12.45$, and Re = 550 and $N = 5.66$) until they finally reach a steady-state value. This decrease of the Lorentz force attests to the formation of vortical structures that reduce the hydrodynamic resistance of the magnetic obstacle (see middle column in Fig. 13). When the Lorentz forces reach a steady state, the magnetic vortices, and therefore the magnetohydrodynamic part of the flow, are fully developed as shown in the right column of Fig. 13, but the flow in the wake is still in a transient stage. For the simulation without stable vortex structure, i.e., for Re = 1100 and $N = 2.83$, no such pronounced decrease to a steady-state value occurs. Only a small minimum appears when the flow is initiated before the Lorentz force also reaches a steady state.

By comparing the Lorentz forces of the fluid to those of the solid slab, one can clearly see that the flow tends to develop in a way that minimizes the acting forces that in turn produce the flow. The difference between the curve of the solid slab and the fluid is directly depending on the flow structure itself. Stable magnetic vortices are most effective in reducing the Lorentz forces, but small-scale vortical structures (i.e., for Re = 1100 and $N = 2.83$) also have a huge impact on the Lorentz force. This observation can be important for industrial applications like Lorentz force velocimetry.

Due to symmetry reasons, the y component of the Lorentz force f_y is almost zero for all cases [see Fig. 12(b)]. The vertical component of the Lorentz force f_z [Fig. 12(c)] first decreases when the magnet approaches the container for all simulations. After passing a minimum, the curves of the Lorentz force diverge and increase to a pronounced maximum when the center of the magnet reaches $x_m \approx 2.0$. This peak is due to the asymmetry of the x component of the magnetic field (see Fig. 5). Here the flow structure influences the Lorentz force only in the initial state, resulting in different values at the maximum. After the magnet moves further in the x direction, the vertical Lorentz forces decrease to steady-state values that are approximatively zero. At this stage, the

(a) $Re = 125$ and $N = 24.91$

$x_m = 0.6$ $x_m = 6.2$ $x_m = 13.8$

(b) $Re = 250$ and $N = 12.45$

$x_m = 0.6$ $x_m = 6.2$ $x_m = 13.8$

(c) $Re = 550$ and $N = 5.66$

$x_m = 0.6$ $x_m = 6.2$ $x_m = 13.8$
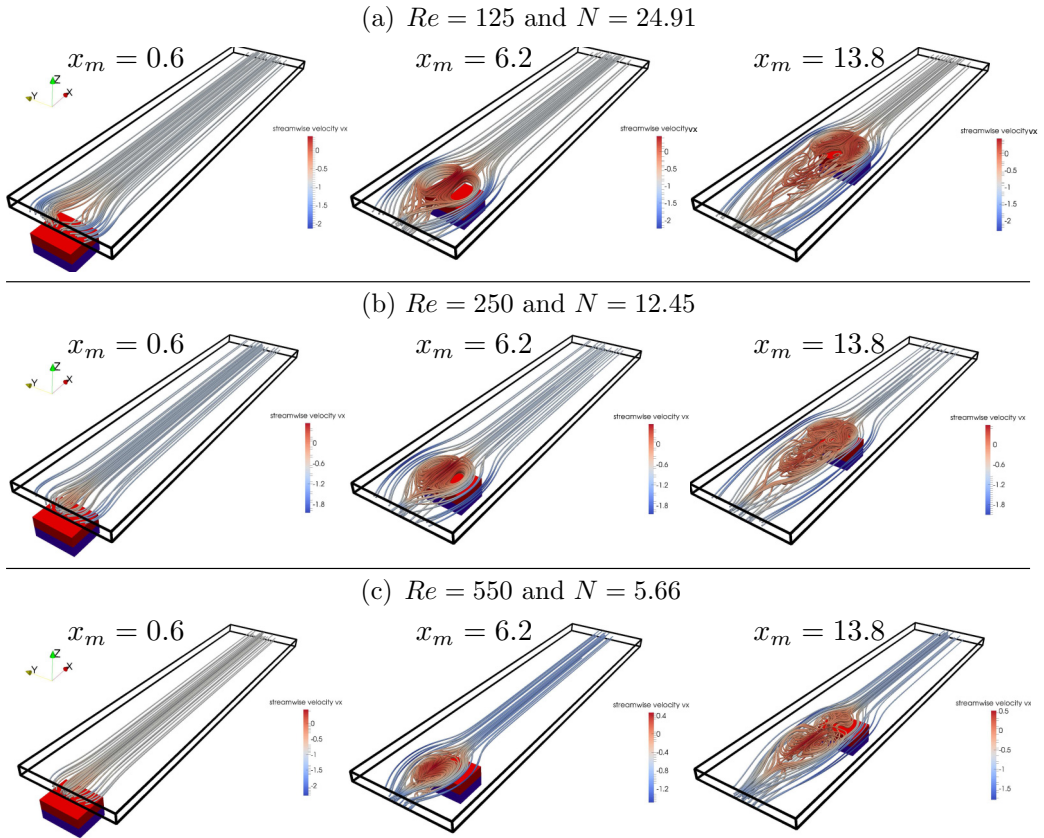
FIG. 13. Transient development (solver B): three-dimensional instantaneous streamlines when the magnet approaches the container and the flow is initiated. Streamlines are properly chosen to demonstrate the main flow structure.

positive and negative values of the x component of the magnetic field intersect the conducting fluid and compensate vertical up- and downward orientated forces. In the extreme case of a solid rod, the vertical component is almost identically zero, while for the fluid simulations the values are slightly higher, which is due to the nonuniform velocity field.

C. Comparison between simulation and experiments

In this section the existing experimental results [14] are presented and compared to the simulations. In the experiments, the flow structure is visualized that occurs on the free surface of the liquid metal, and the Lorentz force is measured that acts on the magnet in the streamwise direction. We recall that the streamlines are visualized by small bubbles which occur at the interface between the liquid metal and the hydrochloric acid solution. A schematic is shown in Fig. 14(a). A photograph of the bubbles is shown in Fig. 14(b), where a standard laboratory glass is filled with GaInSn and covered, analogous to the experiment, with a thin layer of acid solution. Using the diameter of the glass ($d = 60$ mm), we can estimate the diameter of the gas bubbles to be about 0.2 mm.

Figure 15 shows the results for Re $= 125$ and $N = 24.91$. Figure 15(a) shows two-dimensional streamlines obtained from the horizontal velocity components at the surface of the liquid metal layer of the simulation. In Fig. 15(b) the streamlines obtained from the experiment are shown. We can see that the magnetic vortices are in good agreement between the simulation and the experiment. The
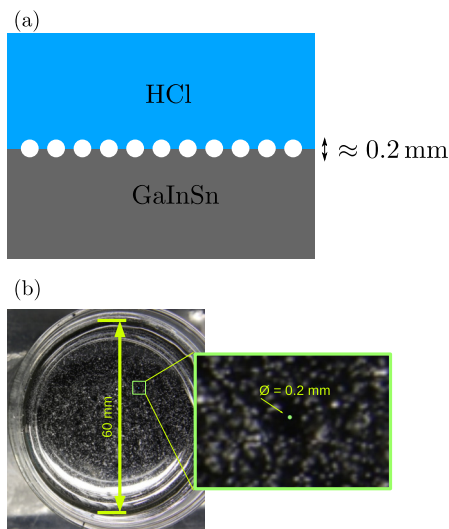
FIG. 14. Experimental method for streamline visualization: (a) schematic of the setup; (b) small gas bubbles arising at the interface due to the interaction of 4% hydrochloric acid solution with the liquid metal.

connecting vortices are similar, but their position and shape differ slightly between the experiment and the simulation. Further downstream the magnetic obstacle, the results obviously differ. While the attached vortices in the experimental picture form closed loops, they do not in the simulation, where they converge into two points.

The mismatch between simulation and experiment can be explained with the previously drawn conclusions, namely, that the flow structure is highly three-dimensional in the wake. In the experiment, the trajectories of the bubbles are forced to be two-dimensional in the interface layer between the liquid metal and the hydrochloric acid solution. Therefore, the bubbles cannot follow the real flow, and the experimental results are misleading.

We now introduce a simplified approach that mimics the movement of the gas bubbles at this interface. In general, the behavior of bubbles at a fluid-fluid interface is a highly complicated multiphase-flow problem, which is beyond the scope of our numerical method and forces us to make some strong assumptions. First, we treat the bubbles as a separate layer above the liquid metal. According to the bubble size, the layer has a thickness of $0.2\,\mathrm{mm}$. We assume this layer to have the same kinematic viscosity as the dilute acid layer, which is approximately the same as that of water $\nu_{\mathrm{acid}} = 1 \times 10^{-6}\,\mathrm{m^2\,s^{-1}}$ [22]. Therefore, the Reynolds number in the interface layer reduces to $\mathrm{Re}_{\mathrm{interface}} = 1.0$ (for $\mathrm{Re} = 125$ and $N = 24.91$), $\mathrm{Re}_{\mathrm{interface}} = 2.0$ (for $\mathrm{Re} = 250$ and $N = 12.45$), and $\mathrm{Re}_{\mathrm{interface}} = 4.4$ (for $\mathrm{Re} = 550$ and $N = 5.66$), respectively. For $\mathrm{Re} = 1100$ and $N = 2.83$ no stable vortex structures occur and results from streamline visualizations are therefore omitted here. Furthermore, we assume a one-way coupling between the liquid metal and the acid solution and hence extract a two-dimensional velocity distribution profile of the surface of a fully evolved liquid metal flow [like shown in Fig. 15(a)] and prescribe it as a fixed tangential velocity distribution at the bottom of the hypothetic interface layer. This velocity distribution is extracted only for one single snapshot of each simulation. Hence, we assume that the flow structure is stationary at the surface of the liquid metal. The boundary condition at the side walls of the interface layer are set to no-slip and at the top to free-slip.

This simplified model can be interpreted as follows. The constant velocity distribution at the bottom boundary of the hypothetic bubble layer, obtained from the surface of the liquid metal, drives a purely hydrodynamic flow inside this interface layer. Due to the increased viscosity and tenuity of the interface layer (and therefore reduced Reynolds number), the flow is forced to be approximately
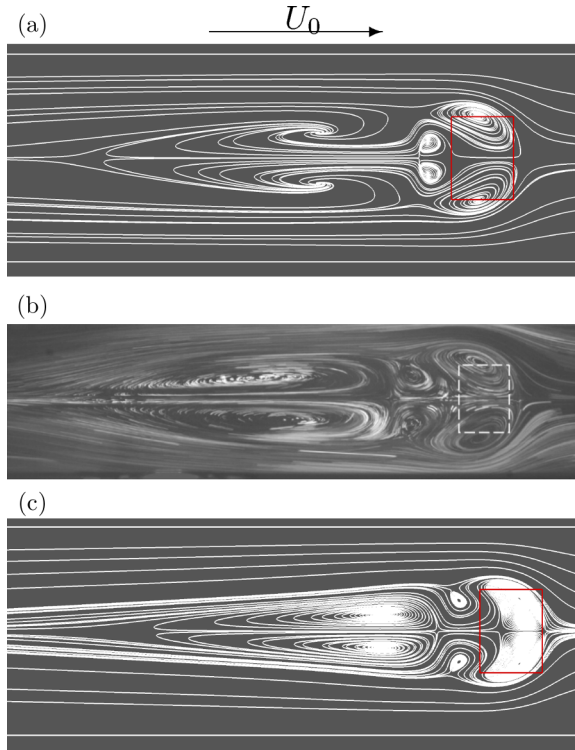
FIG. 15. Two-dimensional streamlines for Re $= 125$ and $N = 24.91$ at the surface of the liquid metal layer (a), obtained from experiment (b), and in the hypothetic bubble interface layer (c); red lines show the contour of the magnet.

two-dimensional. The simulations are performed for several time steps, until the flow structure in the interface layer reaches a steady state.

The two-dimensional streamlines obtained in a horizontal plane roughly in the middle of the hypothetic acid layer are presented in Fig. 15(c). Again, the shape and orientation of the magnetic vortices are in very good agreement with the experimental results. The connecting vortices are shifted downstream, and their shape and position are now in excellent agreement between simulation and experiment. Also the two attached vortices are reproduced by the modified numerical model and agree well in position, size, and shape.

Results for Re $= 250$ and $N = 12.45$ are presented in Fig. 16. Again, two-dimensional streamlines at the surface of the liquid metal are shown obtained from the simulation [Fig. 16(a)] and the experiment [Fig. 16(b)]. The mismatch between both is even worse than in the previous case. The magnetic vortices are similar, but the connecting and attached vortices differ strongly. Again, we use our modified model to reconstruct the movement of the bubbles [Fig. 16(c)]. Similar to the previous cases, the flow structure is in very good agreement between simulation (with the modified model) and experiment. Again, the connecting vortices are shifted downstream with respect to the magnetic obstacle and the attached vortices form closed loops.

Results for Re $= 550$ and $N = 5.66$ are presented in Fig. 17. Here both the streamlines at the surface as well as in the hypothetic bubble layer fail to reproduce the experiment. The experimental results indicate that additional effects occur on the surface in the wake of the obstacle, which might be caused by surface deformation due to the increased velocity of the magnet. It seems plausible that our free-slip approximation at the surface is not valid any more and causes these differences.
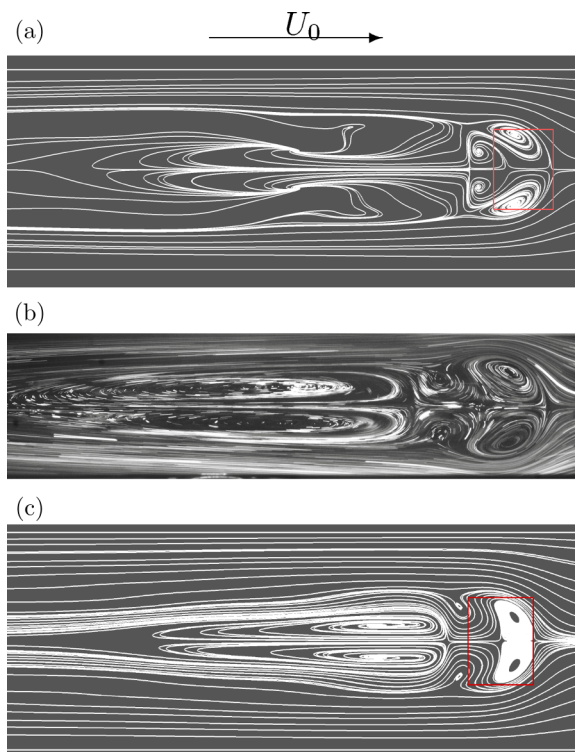
FIG. 16. Two-dimensional streamlines for Re = 250 and $N = 12.45$ at the surface of the liquid metal layer (a), obtained from experiment (b), and in the hypothetic bubble interface layer (c); red lines show the contour of the magnet.

Further available experimental data are the streamwise component of the Lorentz force. Figure 18 shows the numerically and experimentally obtained steady-state values of the Lorentz force for a fully developed flow depending on the Reynolds number in dimensional units. For the realization with the lowest Reynolds number (i.e., Re = 125 and $N = 24.91$) measured data are lacking. In general, the values are in good agreement between simulation and experiment. For Re = 250 and $N = 12.45$, the streamwise Lorentz force is almost identically. For Re = 550 and 1100, the discrepancy is larger, but still in an acceptable range of about 30%.

IV. SUMMARY AND CONCLUSIONS

We investigated the flow structure inside and in the wake of the magnetic obstacle by means of direct numerical simulations for four different cases, i.e., Re = 125 and $N = 24.91$, Re = 250 and $N = 12.45$, Re = 550 and $N = 5.66$, and Re = 1100 and $N = 2.83$, and compared the results to experimental data.

Results from our numerical simulations show that for Re = 125 and $N = 24.91$, as well as for Re = 250 and $N = 12.45$ a so-called six-vortex structure occurs. We find that the attached vortices are highly three-dimensional, while the magnetic vortices in the inner region of the magnetic obstacle are almost two-dimensional, aligned along the vertical direction. For Re = 550 and $N = 5.66$, the regime changes. Inside the magnetic obstacle two less pronounced magnetic vortices occur, and in the wake the stable attached and connecting vortices are replaced by smaller vortical structures. Although no stable attached vortices develop, a region with extensive recirculation appears. For Re = 1100 and $N = 2.83$, no stable vortex structure is present at all. Due to the higher Reynolds
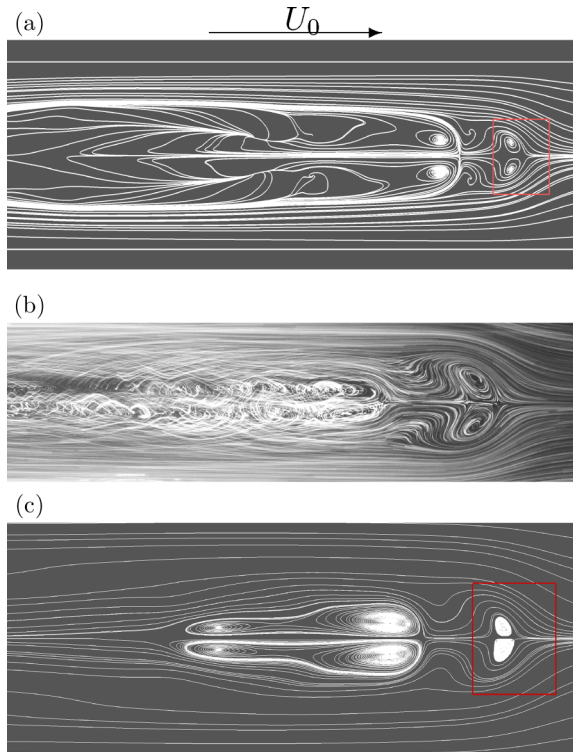
FIG. 17. Two-dimensional streamlines for Re $= 550$ and $N = 5.66$ at the surface of the liquid metal layer (a), obtained from experiment (b), and in the hypothetic bubble interface layer (c); red lines show the contour of the magnet.

number, and therefore the decreased ratio of Lorentz forces to inertia forces, the magnetic obstacle produces only small vortical structures in the far wake of the obstacle.

Furthermore, we analyzed the transient development of the flow, i.e., when the magnet approaches the container and crosses its front wall. As long as the fluid is quiescent, Lorentz forces behave similar
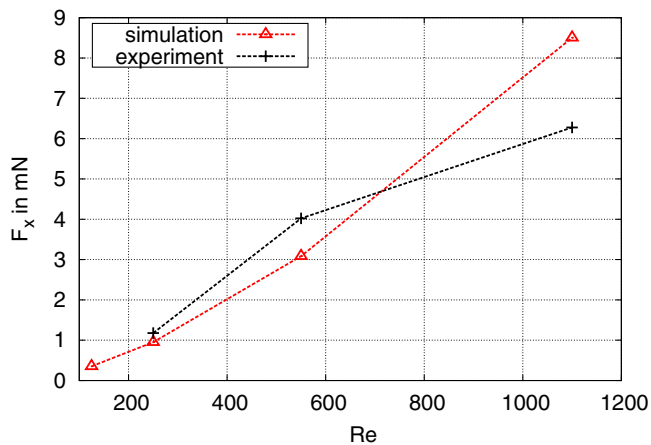
FIG. 18. Comparison between experiment and simulation: streamwise component of the steady-state Lorentz force F_x (in dimensional form) depending in the Reynolds number Re. For Re $= 125$ and $N = 2.83$ measured data are lacking.

to a magnet approaching a solid slab. When the fluid begins to move, vorticity is generated in a way that the acting Lorentz forces are reduced. For stable vortex structures, the Lorentz force is reduced most efficiently, but also for regimes with no stable vortices, the streamwise Lorentz force differs clearly to that of a solid slab. This might be of interest for practical applications like Lorentz force velocimetry.

A direct comparison of the flow structure between our numerical results and the experiments [14] is not possible. We demonstrate that the mismatch is a consequence of the three-dimensionality of the flow structure itself. The experimental technique used for streamline visualization (gas bubbles at the interface between liquid metal and acid solution) is insufficient to picture the correct flow structure, but it at least allows the visualization of the structural changes between the different flow regimes. We underpin our conclusion by introducing a simplified numerical model that tries to mimic the behavior of the gas bubbles at the interface. For this, we treat the region with gas bubbles as a separate layer on top of the liquid metal and assume a one-way coupling between the liquid metal and the hypothetical layer of gas bubbles. Due to the tenuity of this layer in addition to the increased kinematic viscosity, the trajectories of the gas bubbles are forced to be nearly two-dimensional. The flow structure in this hypothetical layer is in excellent agreement with the experimental results for Re = 125 and N = 24.91 and for Re = 250 and N = 12.45. For higher Reynolds numbers, this approach also fails. We assume that surface deformations occur and our simplified free-slip approximation of the free-surface is insufficient to resolve the flow structure accurately at the surface. For future work, it might be interesting to investigate the effects of surface perturbations in a free-surface liquid-metal flow under the influence of a localized magnetic field in an experimental study, as it has been done for electrolytes by Alcalá and Cuevas [23].

Furthermore, measured and simulated values of the streamwise Lorentz force are compared. While they show excellent agreement for Re = 250 and N = 12.45, the agreement for higher Reynolds number is worse, but still within an acceptable level of about 30%. The good reproduction of the Lorentz forces demonstrates the correctness of our numerical method.

For future experiments with this setup, the three-dimensionality of the flow structure should be taken into account. We assume that for a thinner layer of liquid metal the movement of the gas bubbles at the surface of the liquid metal will reflect more accurately the flow structure in the depth of the liquid metal layer.

APPENDIX A: INDUCTION PROBLEM FOR MOVING MAGNET

Let **B** be the imposed magnetic field of the permanent magnet, **b** the magnetic field of the induced currents **j**, $\mathbf{B}_t = \mathbf{B} + \mathbf{b}$ the total magnetic field, and **u** the fluid velocity in the reference system of the laboratory.

Ohm's law for moving conductor reads

$$\mathbf{j} = \sigma[\mathbf{E} + (\mathbf{u} \times \mathbf{B}_t)), \tag{A1}$$

where σ is the electrical conductivity of the fluid. Using Ampère's law ($\nabla \times \mathbf{b} = \mu\mathbf{j}$, where μ is the magnetic permeability of free space) and Faraday's law of induction ($\nabla \times \mathbf{E} = \frac{-\partial \mathbf{B}_t}{\partial t}$), we obtain by taking the curl of Eq. (A1):

$$\nabla \times \nabla \times \mathbf{b} = \mu\sigma\left[-\frac{\partial \mathbf{B}_t}{\partial t} + \nabla \times (\mathbf{u} \times \mathbf{B}_t)\right]. \tag{A2}$$

Equation (A2) is the induction equation. We now make length, time, and velocity nondimensional by introducing the scales L, U, and L/U, and obtain

$$\tilde{\nabla} \times \tilde{\nabla} \times \mathbf{b} = \mathrm{Re}_m \left[-\frac{\partial \mathbf{B}_t}{\partial \tilde{t}} + \tilde{\nabla} \times (\tilde{\mathbf{u}} \times \mathbf{B}_t) \right], \tag{A3}$$

where $\mathrm{Re}_m = \sigma \mu U L$ is the magnetic Reynolds number. The tilde indicates nondimensional operators and quantities. Since $\mathrm{Re}_m \ll 1$, we can express $\mathbf{b}$ by the leading terms of the perturbation ansatz:

$$\mathbf{b} = \sum_{n=0}^{\infty} \mathrm{Re}_m^n \mathbf{b}_n = \mathbf{b}_0 + \mathrm{Re}_m^1 \mathbf{b}_1 + \cdots. \tag{A4}$$

Inserting this ansatz in the nondimensional induction equation (A3), we get for terms with coefficient $\mathrm{Re}_m^0 = 1$:

$$\tilde{\nabla} \times \tilde{\nabla} \times \mathbf{b}_0 = 0. \tag{A5}$$

Since the leading term of the induced current density $\mathbf{j}_0$ is proportional to $\tilde{\nabla} \times \mathbf{b}_0$ (Ampère's law), it follows that $\mathbf{j}_0$ is curl-free and, therefore, can be written as a gradient of a scalar function f:

$$\mathbf{j}_0 = \tilde{\nabla} f. \tag{A6}$$

Ampère's law also implies that $\tilde{\nabla} \cdot \mathbf{j}_0 = 0$. Therefore, f satisfies the Laplace equation

$$\tilde{\nabla}^2 f = 0. \tag{A7}$$

Because the fluid has electrically insulating boundaries ($\mathbf{j} \cdot \mathbf{n} = \frac{\partial f}{\partial n} = 0$), the solution f of (A7) must be constant. Therefore, we have

$$\mathbf{j}_0 = \tilde{\nabla} f = 0. \tag{A8}$$

This absence of electrical currents for $\mathbf{b}_0$ implies that $\mathbf{b}_0$ is identically zero everywhere. The ansatz (A4) becomes

$$\mathbf{b} = \mathrm{Re}_m \mathbf{b}_1. \tag{A9}$$

By inserting this again in Eq. (A3) and considering only terms with coefficient Re_m^1, we have

$$\tilde{\nabla} \times \tilde{\nabla} \times \mathbf{b}_1 = -\frac{\partial \mathbf{B}}{\partial \tilde{t}} + \tilde{\nabla} \times (\tilde{\mathbf{u}} \times \mathbf{B}) \tag{A10}$$

The imposed magnetic field gets advected with the velocity of the magnet $\tilde{\mathbf{u}}_0$:

$$\frac{\partial \mathbf{B}}{\partial \tilde{t}} = -(\tilde{\mathbf{u}}_0 \cdot \tilde{\nabla}) \mathbf{B}. \tag{A11}$$

Further, we have

$$\tilde{\nabla} \times (\tilde{\mathbf{u}}_0 \times \mathbf{B}) = \underbrace{(\mathbf{B} \cdot \tilde{\nabla}) \tilde{\mathbf{u}}_0}_{=0} - (\tilde{\mathbf{u}}_0 \cdot \tilde{\nabla}) \mathbf{B} + \underbrace{\tilde{\mathbf{u}}_0 (\tilde{\nabla} \cdot \mathbf{B})}_{=0} - \underbrace{\mathbf{B}(\tilde{\nabla} \cdot \tilde{\mathbf{u}}_0)}_{=0}. \tag{A12}$$

Inserting Eq. (A12) in Eq. (A11) and the result in Eq. (A10), we obtain

$$\tilde{\nabla} \times \tilde{\nabla} \times \mathbf{b}_1 = \tilde{\nabla} \times [(\tilde{\mathbf{u}} - \tilde{\mathbf{u}}_0) \times \mathbf{B}]. \tag{A13}$$

Since $\mathbf{b} = \mathrm{Re}_m \mathbf{b}_1$, we have

$$\tilde{\nabla} \times \tilde{\nabla} \times \mathbf{b} = \mathrm{Re}_m \{ \tilde{\nabla} \times [(\tilde{\mathbf{u}} - \tilde{\mathbf{u}}_0) \times \mathbf{B}] \}. \tag{A14}$$

Going back to the dimensional formulation and using Ampère's law, we have

$$\nabla \times \mathbf{j} = \sigma \nabla \times [(\mathbf{u} - \mathbf{u}_0) \times \mathbf{B}] \tag{A15}$$
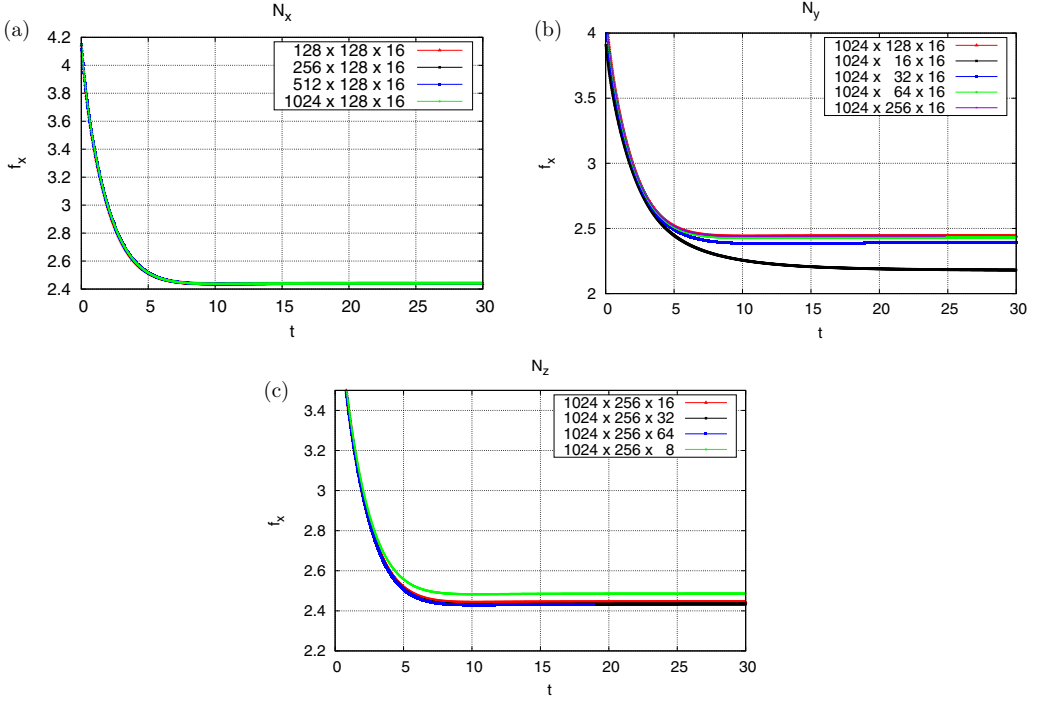
FIG. 19. Grid sensitivity study for solver A for Re $= 1100$ and $N = 2.88$: for (a) N_x, (b) N_y, and (c) N_z.

and therefore

$$\mathbf{j} = \sigma[-\nabla\phi + (\mathbf{u} - \mathbf{u}_0) \times \mathbf{B}].$$ (A16)

APPENDIX B: GRID SENSITIVITY STUDY

Figure 19 shows the results from the grid sensitivity study for solver A (Fishpack) for the highest considered Reynolds number Re $= 1100$ and $N = 2.88$. The convergence is estimated by the streamwise component of the Lorentz force f_x depending on time t. Although Fig. 19 shows that the results are relatively insensitive to the grid resolution, we decided to adopt a resolution
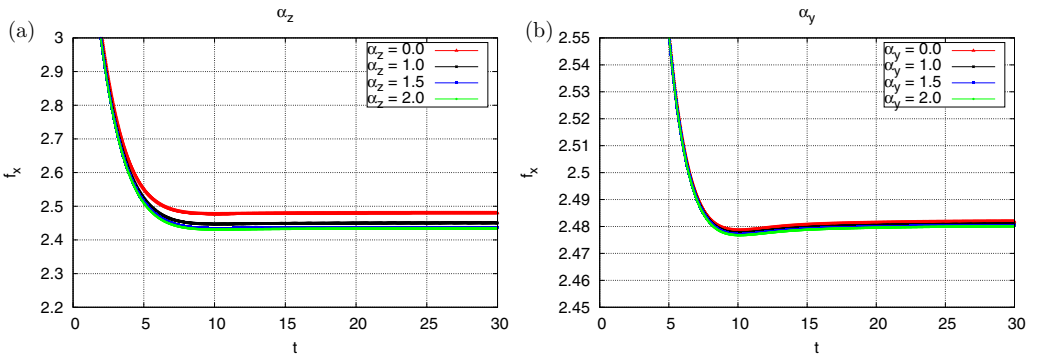
FIG. 20. Grid sensitivity study for solver A for Re $= 1100$ and $N = 2.88$ (grid clustering in the wall normal direction): for (a) α_y and (b) α_z.
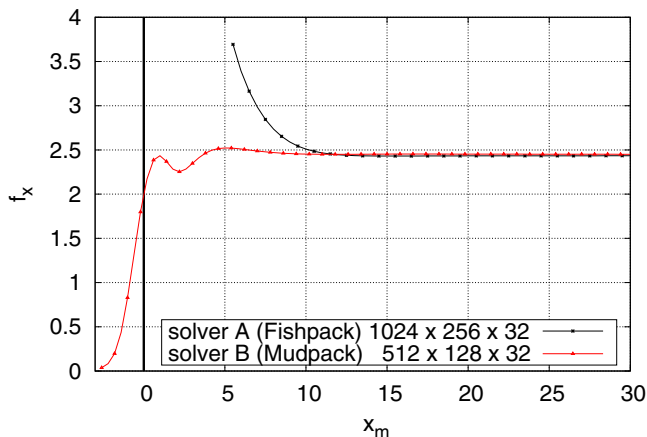
FIG. 21. Grid sensitivity study for solver B for Re $= 1100$ and $N = 2.88$. Shown is a comparison between the steady-state value of the streamwise component of the Lorentz force f_x, obtained from solver A, and the transient development until a steady state is achieved obtained from solver B.

of $1024 \times 256 \times 32$ for $N_x \times N_y \times N_z$. We chose this relatively high resolution because we faced numerical issues for lower resolutions, i.e., the divergence of the velocity field was unacceptably high. This might be due to sharp gradients of the strong localized magnetic field. However, an increase in resolution fixed this issue.

Figure 20 shows a sensitivity study for different levels of grid clustering in the spanwise and vertical directions according to Eq. (17). To accurately resolve the thin magnetohydrodynamic boundary layers, we decided to apply a rather strong grid stretching of $\alpha_y = \alpha_z = 2.0$.

Figure 21 shows a comparison of the steady-state values of the Lorentz force obtained by solver A (Fishpack) and solver B (Mudpack). The values are depending on the spatial position of the magnet x_m. Since solver B cannot be parallelized by domain decomposition and computations are therefore highly time-consuming, we are forced to decrease the grid resolution to $512 \times 128 \times 32$ for $N_x \times N_y \times N_n$. We also shortened the computational domain length in the streamwise direction from 60 to 40 for computations with solver B.

---

[1] P. A. Davidson, *An Introduction to Magnetohydrodynamics* (Cambridge University Press, Cambridge, U.K., 2001).

[2] J. A. Shercliff, *A Textbook of Magnetohydrodynamics* (Pergamon Press, Oxford, U.K., 1965).

[3] P. H. Roberts, *An Introduction to Magnetohydrodynamics* (Longman, London, U.K., 1967).

[4] A. Thess, E. V. Votyakov, and Yu. Kolesnikov, Lorentz Force Velocimetry, Phys. Rev. Lett. **96**, 164501 (2006).

[5] A. Thess, E. Votyakov, B. Knaepen, and O. Zikanov, Theory of the Lorentz force flowmeter, New J. Phys. **9**, 299 (2007).

[6] E. V. Votyakov, E. Zienicke, and Y. B. Kolesnikov, Constrained flow around a magnetic obstacle, J. Fluid Mech. **610**, 131 (2008).

[7] E. V. Votyakov, Yu. Kolesnikov, O. Andreev, E. Zienicke, and A. Thess, Structure of the Wake of a Magnetic Obstacle, Phys. Rev. Lett. **98**, 144504 (2007).

[8] S. Cuevas, S. Smolentsev, and M. A. Abdou, On the flow past a magnetic obstacle, J. Fluid Mech. **553**, 227 (2006).

[9] S. Kenjereš, Energy spectra and turbulence generation in the wake of magnetic obstacles, Phys. Fluids **24**, 115111 (2012).

[10] S. Tympel, T. Boeck, and J. Schumacher, Laminar and transitional liquid metal duct flow near a magnetic point dipole, J. Fluid Mech. **735**, 553 (2013).

[11] E. V. Votyakov and S. C. Kassinos, On the analogy between streamlined magnetic and solid obstacles, Phys. Fluids **21**, 097102 (2009).

[12] A. Beltrán, E. Ramos, S. Cuevas, and M. Brøns, Bifurcation analysis in a vortex flow generated by an oscillatory magnetic obstacle, Phys. Rev. E **81**, 036309 (2010).

[13] F. Samsami, Y. Kolesnikov, and A. Thess, Vortex dynamics in the wake of a magnetic obstacle, J. Visualization **17**, 245 (2014).

[14] Y. Kolesnikov and A. Thess, Experimental investigation of liquid metal flow across a nonhomogeneous magnetic field, in *6th International Conference on Electromagnetic Processing of Materials, 19–23 October 2009, Dresden, Germany*, edited by G. Gerbeth and Y. Fautrelle (2009).

[15] D. Krasnov, O. Zikanov, and T. Boeck, Comparative study of finite difference approaches in simulation of magnetohydrodynamic turbulence at low magnetic Reynolds number, Comput. Fluids **50**, 46 (2011).

[16] E. P. Furlani, *Permanent Magnet and Electromechanical Devices: Materials, Analysis, and Applications* (Academic Press, London, U.K., 2001).

[17] Y. Morinishi, T. S. Lund, O. V. Vasilyev, and P. Moin, Fully conservative higher order finite difference schemes for incompressible flow, J. Comput. Phys. **143**, 90 (1998).

[18] O. Zikanov, D. Krasnov, Y. Li, T. Boeck, and A. Thess, Patterned turbulence in spatially evolving magnetohydrodynamic duct and pipe flows, Theor. Comput. Fluid Dyn. **28**, 319 (2013).

[19] J. C. Adams, P. Swarztrauber, and R. Sweet, Efficient fortran subprograms for the solution of separable elliptic partial differential equations, https://www2.cisl.ucar.edu/resources/legacy/fishpack/ (1999).

[20] J. C. Adams, Mudpack: Multigrid software for elliptic partial differential equations, https://www2.cisl.ucar.edu/resources/legacy/mudpack/ (1999).

[21] J. Jeong and F. Hussain, On the identification of a vortex, J. Fluid Mech. **285**, 69 (1995).

[22] E. Nishikata, T. Ishii, and T. Ohta, Viscosities of aqueous hydrochloric acid solutions, and densities and viscosities of aqueous hydroiodic acid solutions, J. Chem. Eng. Data **26**, 254 (1981).

[23] G. Alcalá and S. Cuevas, Surface waves generated on electrolytes by a traveling electromagnetic force, in *Experimental and Computational Fluid Mechanics* (Springer, Berlin, Germany, 2014), p. 369.